

Nonlinear Interactions of Planetary-Scale Waves in Mesospheric Winds Observed at 52°N Latitude and Two Longitudes

Maosheng He^{1,2}, Jeffrey M. Forbes³, Gunter Stober⁴, Christoph Jacobi⁵,
Guozhu Li^{6,7}, Libo Liu^{6,8}, Jiyao Xu¹

¹Key Laboratory of Solar Activity and Space Weather, National Space Science Center, Chinese Academy of Sciences, Beijing, China

²Hainan National Field Science Observation and Research Observatory for Space Weather, National Space Science Center, Chinese Academy of Sciences, Beijing, China

³Ann & H. J. Smead Department of Aerospace Engineering Sciences, University of Colorado, Boulder, USA

⁴Institute of Applied Physics & Oeschger Center for Climate Change Research, Microwave Physics, University of Bern, Bern, Switzerland

⁵Institute for Meteorology, Leipzig University, Leipzig, Germany

⁶Beijing national observatory of space environment, Institute of Geology and Geophysics, Chinese Academy of Sciences, Beijing, China

⁷College of Earth and Planetary Sciences, University of Chinese Academy of Sciences, Beijing, China

⁸Heilongjiang Mohe National Observatory of Geophysics, Beijing, China

Key Points:

- Planetary wave normal modes drive multi-day oscillations, showing April-October seasonality and statistical SSW associations (not one-to-one)
- First evidence of frequency and zonal wavenumber matching for over 10 secondary waves of nonlinear interactions among planetary-scale waves
- Non-migrating components dominate the winter 24-h tide and summer 8-h tide, attributed to the nonlinear interactions

Corresponding author: Maosheng He, hemaosheng@nssc.ac.cn

Abstract

Nine years of mesospheric wind data from two meteor radars at 52°N latitude were analyzed to investigate planetary waves (PWs) and tides by estimating their zonal wavenumber through longitudinal phase differences. Our results reveal that PW normal modes (NMs) primarily drive multi-day oscillations, showing seasonal variability and statistical associations with Sudden Stratospheric Warming (SSW) events. Specifically, a significant 6-day NM emerges in April, followed by predominant 4- and 2-day NMs until June, with peaks of 2-, 4-, and 6-day NMs spanning July to October. Furthermore, our study provides the first observational verification of frequency and zonal wavenumber of over ten secondary waves from nonlinear interactions among planetary-scale waves. One notable finding is the prevalence of non-migrating components in winter 24-hour and summer 8-hour tides, attributed to these nonlinear interactions. Our findings underscore the diverse nonlinear dynamics of planetary-scale waves, triggering a variety of periodic oscillations.

Plain Language Summary

We analyzed nine years of mid-latitude middle atmospheric wind data at two longitudes. By examining longitudinal phase differences, we identified planetary-scale waves and their sources. Most multi-day oscillations are linked to planetary wave normal modes, influenced by atmospheric mechanical properties. Certain normal modes were prominent from April to October, while others correlated with winter's sudden stratospheric warming events. These modes, along with tides and stationary planetary waves, interact nonlinearly, generating secondary waves of non-normal mode multi-day oscillations and sun-asynchronous tides. Our two-station method reveals for the first time secondary waves of stationary planetary waves, which share the same frequencies as their parent waves, making them indistinguishable in single-station spectral analyses. This phenomenon might explain the prevalence of sun-asynchronous components in the 24-hour winter and 8-hour summer tides, which are exceptions to the typically dominant sun-synchronous tides. Additionally, we report for the first time the interactions of normal modes with non-migrating and 8-hour tides. Our findings highlight the extensive and varied nonlinear behaviors of planetary-scale waves, resulting in a broad spectrum of oscillations.

1 Introduction

Extratropical planetary waves (PWs), also referred to as Rossby waves, play a significant role in the dynamics of rotating fluids, where the meridional gradient of the Coriolis force acts as the restoring force (Zaqarashvili et al., 2021; Holton & Hakim, 2012). In Earth’s atmosphere, PWs exhibit exceptional behavior in the form of normal modes (NMs), intricately linked to the resonant properties of the medium. Constrained predominantly within westerly winds due to Earth’s rotation, PWs manifest a westward phase velocity relative to their carrying fluids, a consequence of the conservation of absolute vorticity. These principles are illustrated in Figure 1 of He and Forbes (2022). The temporal spectrum of PW NMs spans discretely scales from a few days to several weeks, with periods of 2, 4, 5–6, 10, 16, and 25–28 days.

Ground-based observations have proven pivotal in delineating the seasonality of PWs (e.g., Hocking & Kishore Kumar, 2011; Jacobi et al., 2008; Jiang et al., 2008; Sridharan et al., 2006; Gong et al., 2018; F. R. Yu et al., 2019). However, most of these studies relied on single-station analyses, lacking the capacity to measure horizontal scales. Space-based observations, on the other hand, have contributed to investigating the climatology of PWs with constraints on zonal wavenumber (e.g., Gu et al., 2013; Yamazaki et al., 2021; Forbes & Zhang, 2017, 2015; McDonald et al., 2011, respectively) for waves with periods of 2, 4, 6, 10, and 16 days. Nevertheless, these observations, mostly collected in quasi-sun-synchronous orbits and using single-satellite analyses, and are thus susceptible to ambiguities from aliasing, as discussed by Forbes and Zhang (2017). Distinguishing NMs from secondary waves resulting from interactions between NMs and migrating tides is challenging, as elaborated in Section 1 of He, Forbes, et al. (2021).

Recently, using mesospheric wind data observed from two meteor radars at 52°N latitude, He and Forbes (2022) demonstrated that the dominant 2–32-day fluctuations during the 2019 New Year sudden stratospheric warming event (SSW) can be attributed to either PW NMs or their nonlinear behaviors. This analysis determines frequency and zonal wavenumber directly from observations, unlike satellite-based climatological interpretations that often fit individual waves using predetermined frequencies and wavenumbers. Here, we extend this event study to a 9-year window, elucidating PWs’ seasonal variations and statistical occurrences during SSWs. The association between NMs and SSWs remains debated. While some studies affirm this association (Pancheva et al., 2008;

Yamazaki & Matthias, 2019), while others challenge it (Sassi et al., 2012). In addition, our zonal wavenumber estimations facilitate identifying the secondary waves of stationary PW (sPW) interactions with migrating tides and NMs which are indistinguishable in single-station spectral analyses as they have the same frequencies as the parent tides and NMs.

2 Data Analysis

The data utilized in this study are comprised of observations of mesosphere winds spanning from 2012 to 2020, obtained from two meteor radars situated at comparable latitudes but separated in longitude by 109° . One station is positioned in Mohe at coordinates 122°E , 53.5°N (Y. Yu et al., 2013), while the second is situated in Collm, coordinates 13.0°E , 51.3°N (Jacobi, 2012; Stober et al., 2021, 2022). Employing the methodology delineated by (Hocking et al., 2001; Holdsworth et al., 2004) for the SKiYMET and ATRAD meteor radars, respectively, zonal and meridional wind components (u and v) are computed on an hourly basis within an altitude range spanning from 80.5 km to 95.5 km.

2.1 Estimation of Zonal Wavenumber

Following the methodology employed in Figure 2 of He and Forbes (2022), the cross spectra between Mohe and Collm are computed for horizontal winds, as illustrated in Figure 1. This procedure involves computing cross-wavelet spectra of the zonal (u) and meridional (v) wind components separately at each altitude level, followed by summing these spectra and subsequently averaging the resultant sum across all altitudes. The cross spectrum enables the estimation of the zonal wavenumber (s) associated with the underlying wave, employing the phase difference technique (PDT).

Similar to other discrete spectral analyses, the PDT involves several assumptions, including adherence to the Nyquist sampling theorem. This principle dictates that the sampling frequency in both temporal and spatial domains must exceed twice the maximum frequency and wavenumber inherent in the signal. However, validating these assumptions through models is intrinsically insufficient, as sufficient validation necessitates complete knowledge of the signal, particularly its components at frequencies and wavenumbers surpassing the Nyquist rates, which often pose significant modeling challenges. In

the PDT framework, prior knowledge allows a partial relaxation of the assumption regarding the Nyquist rate in space, as discussed in the context of the "long-wave assumption" by He, Chau, et al. (2020). Notably, this assumption's relaxation varies across scenarios, often guided by a predefined set of potential s . The current study uses the relaxations defined in He and Forbes (2022) and He et al. (2024) in dealing with the inter- and intra-diurnal spectra, respectively. These relaxations primarily aim to identify the simplest explanation among potential aliasing candidates beyond the Nyquist rate.

Another crucial assumption concerns the constraints of linear systems, where solving for a given number of unknowns necessitates an equal number of equations. Sampling from N locations enables the estimation of wave amplitudes for up to N different predefined wavenumbers within a specified time-frequency grid. In existing literature, the prevailing approach to studying the upper mesosphere involves $N = 1$ analyses, conducted via single-station or -satellite spectral methods. These analyses operate under the single-wave assumption, presuming the presence of only one predominant wave within each discernible time-frequency grid. Consequently, in $N = 1$ analyses, estimating wavenumber in the detector's intrinsic coordinate system is infeasible, and wavenumber explanation is based on prior knowledge. Observations from an additional location allow for verifying the applicability of the single-wave assumption, for example, by comparing the phase difference between the locations with its expectation associated with the expected wavenumber. In practical applications in the PDT, this verification does not rely on the wavenumber expectation. Since different wave modes typically exhibit distinct evolutions in the time and frequency domains, the superposition of different wave modes is accompanied by phase differences that vary with time and frequency. This characteristic can be used to identify breaches in the single-wave assumption, as illustrated in Section 4.2. Conversely, a stable phase difference over time and frequency indicates that the single-wave assumption is being met. This phase difference is a function of the wavenumber and the separation between locations, thereby allowing for wavenumber estimation. Readers are referred to He (2023) for a review of the PDT approach implemented in a series of works involving both case and statistical studies, including PDT cross-validations using independently paired stations and consistent comparisons with estimations from three- or four-station analyses (He, Forbes, et al., 2020; He, Chau, et al., 2021).

2.2 Composite Analysis

The spectra illustrated in Figure 1 are composited with regard to the day of year and to the central days of SSWs are delineated in Figures 2a–2d and 2e–2h, respectively. The identified central days, marked by vertical dashed lines in Figure 1, are as follows: 17-01-2012, 11-01-2013, 05-01-2015, 06-03-2016, 02-02-2017, 14-02-2018, and 31-12-2018. These reference days are determined based on the occurrences of polar vortex weakening events (PVWs), discerned through the analysis of eastward wind variation at 48 km altitude and 70°N latitude, utilizing MERRA reanalysis data (Zhang & Forbes, 2014).

3 Results

Figure 1a presents the cross-wavelet spectrum for periods $T = 40\text{h}–36\text{d}$ from 2012 to 2020, in which the color intensity denotes the amplitudes, while hue indicates the phase difference between the Mohe and Collm radars, aiding in the estimation of the zonal wavenumber s for dominant waves. Red, green, and blue hues correspond to wavenumbers $s = 1, 2, \text{ and } 3$, respectively. The estimated s , labeled at some dominant peaks as Arabic numerals "1" and "2" for $s = 1$ and 2, shows dependence on the period T , with most red peaks occurring at periods $T > 5\text{d}$, while green peaks predominate at $3 < T < 5\text{d}$. For $T < 3\text{d}$, spectral peaks vary in color and predominantly appear in summer.

3.1 Seasonal Composite of Multi-day Spectra

Seasonal variations are detailed in the composite analyses in Figure 2a, where the most intense spectral peaks emerge in the summer half-year (from April to October), mostly at periods $T \leq 6\text{d}$. The summer spectral peaks manifest a distinct V-shaped distribution. From March to June, the predominant peaks exhibit monotonically decreasing periods (from $T = 6$ days sequentially decreasing to 4, then 2 days), while the wavenumber sequentially increases from $s = 1$ to 2, then 3. Subsequently, from July to October, the predominant peaks show an opposite trend: the period monotonically increases while the wavenumber decreases. This period-wavenumber elucidation of PW seasonality, covering periods greater than 3 days, is reported here for the first time.

Figure 2a furthermore unveils a magenta peak in July–August, at a period $T < 3\text{d}$. This peak may involve multiple quasi-two-day waves, as discussed in (He, Forbes, et al., 2021), to which readers are referred for a comprehensive understanding of year-

to-year and seasonal variability in the spectral segment with $T < 3d$. We will not reiterate these aspects here.

3.2 SSW Composite of Multi-day Spectra

Unlike summer, when the spectrum exhibits significant seasonality, the winter half-year (from November to February) manifests sporadic spectral peaks with diminished amplitudes. Notably, a conspicuous pattern is not readily discernible in Figure 2a during the winter half-year. Instead, the winter spectrum prominently reveals a dependence on SSWs, as evidenced, for instance, in Figure 1a for the early months of 2013, early 2018, and late 2018, where the spectra exhibit pronounced multi-peaks. The SSW composite spectrum manifests peaks at $T = 16, 10, 8, 6, 4,$ and 2 days, as indicated by the digits or symbols '1', '1', '2', '1', '?' and '?' in Figure 2e, respectively. The first four digits identify the wavenumber s diagnosed through the PDT, while the question symbols "?" denote failures of wavenumber diagnosis. These failures are attributed to the mixing of waves with different wavenumbers, a discussion of which is provided in Section 4.

3.3 Near-24-, 12-, and 8-hour Spectra and Their Composites

Figures 1b–1d depict spectra similar to Figure 1a but spanning the frequency ranges 1.00 ± 0.25 cycles per day (cpd), 2.00 ± 0.25 cpd, and 3.00 ± 0.25 cpd, respectively. The composites of these spectra are illustrated in Figures 2b–2d and 2f–2h, with respect to the calendar month and the SSW reference days, respectively. In these representations and for most years, the 24-, 12-, and 8-hour spectra predominantly appear in red, green, and blue, indicating modes $s = 1, 2,$ and $3,$ respectively. These modes correspond to the diurnal, semidiurnal, and terdiurnal migrating tides.

Diverging from these migrating tidal signatures and as indicated by the string '2e' in Figure 2b, the 24-hour spectrum exhibits a prevalence of green hues in November–December, suggesting $s = 2,$ which is a signature of a non-migrating tide. Similarly, a non-migrating signature appears also at the period $T = 8h.$ As indicated by the question symbol "?" in Figure 2d, the 8-hour peak is not in blue colors in May–August but rather exhibits a complex color attributed in Section 4 to mixing of waves with different wavenumbers. In Figure 2g, following the vertical dashed line at $T = 12.4h,$ a green peak emerges, indicating $s = 2,$ and implying a migrating semidiurnal lunar tide (Forbes & Zhang, 2012;

He & Chau, 2019) , though alternative explanations were also argued (van Caspel et al., 2023; Fuller-Rowell et al., 2016).

Additionally, flanking the 24-, 12-, and 8-hour migrating tidal signatures in Figures 1 and 2 are scattered off-24-, 12-, and 8-hour spectral peaks, which will be further discussed in the subsequent section.

4 Discussions

Section 3 illustrated temporal variations of oscillations at the periods of multiple days, and near-24, -12, and -8 hours. The spectra are composited to highlight the seasonal variations and the statistical associations with SSW, and PDT is used to diagnose the zonal wavenumbers of underlying waves. The current section discusses the associated dynamics. Hereafter, we employ a pair of numbers enclosed in square brackets to denote waves, $[\frac{f}{1\text{cpd}}, s]$, where $\frac{f}{1\text{cpd}}$ identifies the frequency in cpd, and s signifies the zonal wavenumber.

4.1 Normal Modes

Most of the multi-day spectral peaks mentioned above can be attributed to the 16-, 10-, 6-, 4-, and 2-day PW NMs or Rossby gravity NMs, $[\frac{1}{16}, 1]$, $[\frac{1}{10}, 1]$, $[\frac{1}{6}, 1]$, $[\frac{1}{4}, 2]$, and $[\frac{24}{50}, 3]$ (for details, see Forbes et al., 1995; Forbes, 1995, 1995; Yamazaki et al., 2021; He, Forbes, et al., 2021, respectively). Note that these frequencies represent the NMs in average observations, which differs from the intrinsic frequencies anticipated by classical theory due to the Doppler shift associated with the background wind. Hence, observations of these waves are often prefaced with "quasi-", such as quasi-16-day and quasi-6-day waves. For instance, the $[\frac{1}{16}, 1]$ mode can be anticipated in the range $11 < T < 20$ days based on Salby (1981), providing an explanation for all spectral peaks with wavenumber $s = 1$ within this period range in Figure 1a. The enhancements of the quasi-6-, 4-, and 2-day NMs in the summer-half year have been investigated individually in various datasets (e.g., Riggin et al., 2006; Yamazaki et al., 2021; He, Forbes, et al., 2021, respectively). Here, Figure 2a reveals the seasonal variation of NMs with a single dataset in a single analysis. Apart from these NMs, Figure 1a also displays signatures of other NMs. For example, the red spectral peak ($s = 1$) near $T = 30\text{d}$ in February 2018 and the green spectral peak ($s = 2$) near $T = 7\text{d}$ in February 2019 can be attributed to the 28-day (Zhao et al., 2019) and 7-day NMs (Pogoreltsev et al., 2002), respectively.

In Figures 1a and 2a, a distinct winter-summer contrast emerges in the frequency distribution of NMs. Short-period NMs ($T \leq 6$ days) predominantly manifest during summer, while longer-period NMs ($T > 6$ days) are more prevalent in winter. This seasonal contrast can be qualitatively explained in terms of the longitudinal average of the zonal wind (\bar{u}) and its influence on the PW phase velocity (c) as encapsulated by the inequalities $0 < \bar{u} - c < \bar{u}_{\text{cri}}$ (Charney & Drazin, 1961). The first inequality $0 < \bar{u} - c$ dictates westward propagation of PWs with respect to the background flow, determined by Earth's rotation and the associated north-south gradient of relative vorticity (Rossby, 1939; Andrews et al., 1987; He & Forbes, 2022). The second inequality, defining a threshold (the critical velocity \bar{u}_{cri}) of $\bar{u} - c$, ensures a reversible distortion of potential vorticity contours. Beyond this threshold, the distortion becomes pronounced and irreversible, impeding PW propagation and leading to breaking. In the middle atmosphere at middle latitudes, the difference in \bar{u} between winter and summer primarily manifests as $\bar{u}_{\text{summer}} < \bar{u}_{\text{winter}}$, with westerly $\bar{u}_{\text{winter}} > 0$ during winter and easterly $\bar{u}_{\text{summer}} < 0$ during summer (Jacobi et al., 2009). Combining both $0 < \bar{u} - c < \bar{u}_{\text{cri}}$ and $\bar{u}_{\text{summer}} < \bar{u}_{\text{winter}}$, it is reasonable to anticipate $\bar{c}_{\text{summer}} < \bar{c}_{\text{winter}}$, implying that the winter atmosphere allows NMs with larger c compared to those permitted in summer. Note that since \bar{c} is predominantly negative, larger \bar{c} during winter than summer indicates that waves in winter travel at a slower absolute velocity than in summer. In Figures 1a and 2a, the NMs prevalent in the winter half-year include, for instance, the 28-, 16-, and 10-day NMs associated with $c = -9.7, -17.0,$ and -27.2 m/s, respectively, which are larger (namely slower) than the $c = -45.4, -34.0,$ and -45.4 m/s of the 6-, 4-, and 2-day NMs predominantly observed in the summer half-year. It is noteworthy that the phase velocity is defined in the Earth-fixed frame as $c := \frac{2\pi a \cos \phi}{-sT}$, where $a = 6370$ km defines the Earth's radius, ϕ represents the latitude, and the negative symbol preceding s indicates that a positive c or u denotes eastward motion, opposite to the positive s direction. Also note that for the qualitative discussion above, we disregarded the dependence of \bar{u}_{cri} on NMs' horizontal wavelength.

During SSWs, \bar{u} undergoes a rapid transition from westerly to easterly within a short span of time. This reversal isn't uniform; \bar{u} may stall at certain values for a while, resembling potentially winter- or summer-like conditions. Moreover, the progression of \bar{u} reversal varies across events, facilitating potentially the occurrence of winter- or summer-preferred NMs, as evidenced in Figure 2e. While sPWs are known to play a critical role

in initiating SSWs (Matsuno, 1971), the involvement of NMs in SSWs remains contentious. Some studies support the link between NMs and SSWs (Pancheva et al., 2008; Yamazaki & Matthias, 2019; He, Yamazaki, et al., 2020), while others do not (Sassi et al., 2012). The results presented in our Figures 1 and 2 demonstrate a clear association from a statistical perspective rather than a one-to-one correspondence. Figure 1a shows that not every SSW is associated with NMs, and not all winter PWs are accompanied by SSWs. Our study contributes to resolving the debate over the association between NMs and SSWs.

While NMs effectively account for the majority of significant spectral peaks observed in Figures 2a and 2e, a limited number of exceptions occur. The first two exceptions are the near-2-day spectral peaks, in magenta and cyan in Figures 2a and 2e, respectively, both of which are denoted by the question marks "?" in the Figures. Each of these peaks may comprise multiple wave components. Specifically, the magenta peak may consist of waves with wavenumber $s = 4$ and -2 , while the cyan peak may involve $s = 3$ and 2 (for details see He, Forbes, et al., 2021; He, Chau, et al., 2021, respectively). A third exception is discerned in the peak at $T = 4$ days in Figure 2e, which may also entangle multiple spectral signatures, e.g., the red and green spectral peaks around SSWs 2012/2013 and 2018/2019 in Figure 1a, respectively. The green color suggests $s = 2$ and is attributable to the NM $[\frac{1}{4}, 2]$, whereas the red color might result from the contamination of the NM $[\frac{1}{6}, 1]$. This speculation of contamination is founded on Figure 1a, where, during the 2012/2013 SSW, a singular spectral peak of almost uniform color spans from $T = 4$ day to $T = 6$ day, encompassing phase signals of both 6- and 4-day waves in principle. The last exception is the green peak at $T = 8$ days in Figure 2e which will be detailed in Section 4.2.

4.2 Nonlinear interactions

Non-NM multi-day spectral peaks

In addition to the previously mentioned NMs, Figure 1a contains spectral peaks with $s = 2$ that cannot be explained solely in terms of NMs but rather through secondary nonlinear interactions between different PWs. For an in-depth understanding of secondary non-linearity, readers are referred to He and Forbes (2022). Through such interactions, two waves may generate two new waves, denoted as: $[\frac{f_1}{1cpd}, s_1] \pm [\frac{f_2}{1cpd}, s_2] = [\frac{f_1 \pm f_2}{1cpd}, s_1 \pm s_2]$. Here, '1' and '2' index the parent waves, while '+' and '-' denote sec-

ondary waves, known as upper sideband (USB) and lower sideband (LSB), respectively. In Figure 1a, the green peaks indicated by '2a+', '2b+', and '2c+' are associated with estimation $s = 2$ and could be explained as the USB of interactions between NMs $[\frac{1}{8}, 1]$, $[\frac{1}{10}, 1]$, and $[\frac{1}{16}, 1]$ with sPWs $[0, 1]$ as specified in Lines (a+), (b+), and (c+) in Table 1, respectively. Here, a potential aliasing for the $s = 2$ estimation is $s = -1$, differing by only 33° in the color phase on the color map in Figure 1a. These $s = -1$ aliases should not be neglected as they could be explained as the LSB of the nonlinear interactions of the previous NMs with the sPW as specified in Lines (a-), (b-), and (c-) in Table 1. Both $[0, 1]$ and $[0, 2]$ are frequently observed, though the $[0, 1]$ amplitude is statistically significantly stronger than the $[0, 2]$ (Shi et al., 2021; Smith, 1997). Superposition between the green LSB- or SBU-like SWs ($s = -1$ or 2) with the red NM peaks ($s = 1$) could further explain the spectral peaks arrowed in Figure 1a in 2015. These peaks exhibit complex colors, a combination of red, green, and yellow, which could be attributed to the overlapping of a red and a green peak with distinct evolution in the time and frequency domains. Such superposition between the SW-like wave and the NMs was reported in satellite data (Ma et al., 2024).

In addition, the green peak labeled as '2d' at $T = 8$ days in Figure 2e could be attributed to secondary harmonic generation of an NM as reported by He and Forbes (2022) and specified in Line (d) in Table 1. Figure 1a might also incorporate signatures of more nonlinear interactions, and our intention is to discuss the most typical ones rather than to provide an exhaustive list.

Non-migrating tidal signatures

Section 3.3 illustrated that while the 24-, 12-, and 8-hour spectra are dominated by migrating components $[1, 1]$, $[2, 2]$, and $[3, 3]$, there are also signatures of non-migrating tides. Specifically, the 24-hour green peak in December in Figure 2b can be explained in term of the interaction between the diurnal migrating tide and a sPW, $[0, 1]$, as specified in Line (e) Table 1. Similarly, the 8-hour green and red peaks in June 2020 and May 2015, indicated by the strings '2g' and '4f' in Figure 1d, can be explained as the LSB and USB of the interactions between the tide $[3, 3]$ and the sPW $[0, 1]$, as specified in Lines (f, g) in Table 1, respectively. The superposition of these secondary waves could account for the non-migrating tidal signature in Figure 2d that is indicated by the question symbol (?).

Tidal sidebands

In Figures 2b–2d, sporadic isolated spectral peaks are observed at off-12-hour periods. These peaks are commonly interpreted as secondary waves of interactions between tides and NMs. In Figure 2g, the red peaks, labeled '1m' and '1l' and associated with $s = 1$, signify the LSBs of interactions between the 12-hour migrating tide and NMs as specified in Lines (m,l) of Table 1. In contrast, the blue peaks, labeled '3n', '3o', and '3p' and associated with $s = 3$, represent the corresponding USBs specified in Lines (n–p) of Table 1. Similarly, the green peaks labeled '2h', '2i', and '2j' in Figure 2f, and the green and red peaks labeled '2q', '2r', '2s', and '4t' in Figure 2h, signify the nonlinear sidebands of diurnal and terdiurnal tides, as specified in Lines (h–k) and (q–t) of Table 1, respectively. Additionally, these '3k' and '4t' signatures in Figures 2f and 2h are attributable to non-migrating tidal sidebands of the interactions specified in Lines (f) and (h) of Table 1, respectively.

In existing literature using ground observations, the existence of tidal sidebands is primarily inferred from frequency matching. Here, we demonstrate the existence of sidebands based on both frequency and zonal wavenumber matching. Compared to the more commonly reported off-12-hour tidal sidebands, off-24-hour and off-8-hour sidebands are rarely, if ever, observed in the midlatitude mesosphere. Specifically, we present observational evidence for the NM nonlinear interactions with non-migrating tides and 8-hour tides for the first time. The novelty of these findings is highlighted in Table 1.

5 Conclusion

Utilizing meteor radar observations spanning nine years at two longitudes and 52°N latitude, this study investigates planetary-scale waves in mesospheric winds. By examining zonal wavenumbers s across various time scales (multi-day, near-24-hour, -12-hour, and -8-hour), we distinguished NMs from other PWs, identified migrating and non-migrating tides, and diagnosed a variety of novel nonlinear interactions. Our statistical analysis revealed that PWs were primarily linked to NMs, which exhibit a specific period/wavenumber seasonality during the summer half-year and a winter association with SSWs. Notably, April showcased a prominent 6-day NM (with $s = 1$), followed by a prevalence of 4- and 2-day NMs (with $s = 2$ and $s = 3$, respectively) extending through June. Subsequent peaks in 2-, 4-, and 6-day NMs (with $s = 3$, $s = 2$, and $s = 1$, respectively) were ob-

served from July to October. Our insights into seasonal variations are derived from observational determinations of frequency and zonal wavenumber, contrasting with satellite observations that often rely on fitting individual waves using predetermined frequencies and wavenumbers. Our findings on the statistical association between NMs and SSWs significantly contribute to resolving the ongoing debate on this topic. Additionally, for the first time, we identified evidence of frequency and zonal wavenumber matching for more than ten secondary waves resulting from nonlinear interactions among NMs (16-, 10-, and 6-day), tides (diurnal, semidiurnal, and terdiurnal; migrating and non-migrating), and sPWs. These interactions represent three novel categories involving parent waves of sPWs, terdiurnal tides, and non-migrating tides. The sPW interactions could explain our finding that non-migrating tidal amplitudes surpass the corresponding migrating tides observed in the winter diurnal tide and summer terdiurnal tide. These non-migrating signatures are notable exceptions, as migrating components generally dominate diurnal, semidiurnal, and terdiurnal tides for most months.

Open Research

The hourly wind data from Mohe is provided by the Data Center for Geophysics, National Earth System Science Data Sharing Infrastructure at Beijing National Observatory of Space Environment, Institute of Geology and Geophysics, Chinese Academy of Sciences). The hourly wind data at Mohe and Collm are available in the World Data Center (He, 2020) for Geophysics, Beijing, and Harvard Dataverse (He et al., 2023).

Acknowledgments

This work is supported by the Chinese Meridian Project and the Specialized Research Fund for State Key Laboratory in China. Christoph Jacobi is supported by Deutsche Forschungsgemeinschaft grants JA 863/47-1. Gunter Stober is a member of the Oeschger Center for Climate Change Research. The authors declare that they have no competing financial interests.

References

- Andrews, D. G., Holton, J. R., & Leovy, C. B. (1987). *Middle Atmosphere Dynamics*. Academic Press. (Google-Books-ID: N1oNurYZefAC)
- Charney, J. G., & Drazin, P. G. (1961). Propagation of planetary-scale dis-

- turbances from the lower into the upper atmosphere. *Journal of Geophysical Research (1896-1977)*, 66(1), 83-109. Retrieved from <https://agupubs.onlinelibrary.wiley.com/doi/abs/10.1029/JZ066i001p00083>
doi: <https://doi.org/10.1029/JZ066i001p00083>
- Forbes, J. M. (1995). Tidal and planetary waves. *Geophysical Monograph Series*, 87, 67–87. Retrieved from <http://www.agu.org/books/gm/v087/GM087p0067/GM087p0067.shtml> doi: 10.1029/GM087p0067
- Forbes, J. M., Hagan, M. E., Miyahara, S., Vial, F., Manson, A. H., Meek, C. E., & Portnyagin, Y. I. (1995). Quasi 16-day oscillation in the mesosphere and lower thermosphere. *Journal of Geophysical Research*, 100(D5), 9149. Retrieved from <http://doi.wiley.com/10.1029/94JD02157> doi: 10.1029/94JD02157
- Forbes, J. M., & Zhang, X. (2012). Lunar tide amplification during the January 2009 stratosphere warming event: Observations and theory. *Journal of Geophysical Research: Space Physics*, 117(12), 1–13. doi: 10.1029/2012JA017963
- Forbes, J. M., & Zhang, X. (2015). Quasi-10-day wave in the atmosphere. *Journal of Geophysical Research*, 120(21), 11,079–11,089. doi: 10.1002/2015JD023327
- Forbes, J. M., & Zhang, X. (2017). The quasi-6 day wave and its interactions with solar tides. *Journal of Geophysical Research: Space Physics*, 122(4), 4764–4776. Retrieved from <http://doi.wiley.com/10.1002/2017JA023954> doi: 10.1002/2017JA023954
- Fuller-Rowell, T. J., Fang, T.-W., Wang, H., Matthias, V., Hoffmann, P., Hocke, K., & Studer, S. (2016). Impact of Migrating Tides on Electrodynamics During the January 2009 Sudden Stratospheric Warming. In *Ionospheric Space Weather* (pp. 163–174). American Geophysical Union (AGU). Retrieved 2024-02-04, from <https://onlinelibrary.wiley.com/doi/abs/10.1002/9781118929216.ch14> (Section: 14 _eprint: <https://onlinelibrary.wiley.com/doi/pdf/10.1002/9781118929216.ch14>) doi: 10.1002/9781118929216.ch14
- Gong, Y., Li, C., Ma, Z., Zhang, S., Zhou, Q., Huang, C., ... Ning, B. (2018). Study of the Quasi-5-Day Wave in the MLT Region by a Meteor Radar Chain. *Journal of Geophysical Research: Atmospheres*, 123(17), 9474–9487. Retrieved 2024-02-09, from <https://onlinelibrary.wiley.com/doi/abs/10.1029/2018JD029355> (_eprint:

- <https://onlinelibrary.wiley.com/doi/pdf/10.1029/2018JD029355> doi:
10.1029/2018JD029355
- Gu, S. Y., Li, T., Dou, X., Wu, Q., Mlynczak, M. G., & Russell, J. M. (2013). Observations of Quasi-Two-Day wave by TIMED/SABER and TIMED/TIDI. *Journal of Geophysical Research Atmospheres*, *118*(4), 1624–1639. doi:
10.1002/jgrd.50191
- He, M. (2020). *The hourly mesospheric winds over mohe between 2012 and 2019*. WDC for Geophysics, Beijing. doi: 10.12197/2020GA016
- He, M. (2023, April). Planetary-scale MLT waves diagnosed through multi-station methods: a review. *Earth, Planets and Space*, *75*(1), 63. Retrieved 2023-07-11, from <https://doi.org/10.1186/s40623-023-01808-5> doi: 10.1186/s40623-023-01808-5
- He, M., & Chau, J. L. (2019). Mesospheric semidiurnal tides and near-12h waves through jointly analyzing observations of five specular meteor radars from three longitudinal sectors at boreal midlatitudes. *Atmospheric Chemistry and Physics*, *19*(9), 5993–6006. Retrieved from <https://doi.org/10.5194/acp-19-5993-2019> doi: 10.5194/acp-19-5993-2019
- He, M., Chau, J. L., Forbes, J. M., Thorsen, D., Li, G., Siddiqui, T. A., ... Hocking, W. K. (2020). Quasi-10-Day Wave and Semidiurnal Tide Nonlinear Interactions During the Southern Hemispheric SSW 2019 Observed in the Northern Hemispheric Mesosphere. *Geophysical Research Letters*, *47*(23), e2020GL091453. Retrieved from <https://doi.org/10.1029/2020GL091453> doi: 10.1029/2020GL091453
- He, M., Chau, J. L., Forbes, J. M., Zhang, X., Englert, C. R., Harding, B. J., ... Makela, J. J. (2021). Quasi-2-Day Wave in Low-Latitude Atmospheric Winds as Viewed From the Ground and Space During January–March, 2020. *Geophysical Research Letters*, *48*(13). Retrieved from <https://doi.org/10.1029/2021GL093466> doi: 10.1029/2021GL093466
- He, M., Chau, J. L., Hall, C. M., Tsutsumi, M., Meek, C., & Hoffmann, P. (2018). The 16-Day Planetary Wave Triggers the SW1-Tidal-Like Signatures During 2009 Sudden Stratospheric Warming. *Geophysical Research Letters*, *45*(22), 12,631–12,638. Retrieved from <https://doi.org/10.1029/2018GL079798> doi: 10.1029/2018GL079798

- He, M., Chau, J. L., Stober, G., Li, G., Ning, B., & Hoffmann, P. (2018). Relations Between Semidiurnal Tidal Variants Through Diagnosing the Zonal Wavenumber Using a Phase Differencing Technique Based on Two Ground-Based Detectors. *Journal of Geophysical Research: Atmospheres*, *123*(8), 4015–4026. Retrieved from <https://doi.org/10.1002/2018JD028400> doi: 10.1002/2018JD028400
- He, M., & Forbes, J. M. (2022, December). Rossby wave second harmonic generation observed in the middle atmosphere. *Nature Communications*, *13*(1), 7544. doi: 10.1038/s41467-022-35142-3
- He, M., Forbes, J. M., Chau, J. L., Li, G., Wan, W., & Korotyshkin, D. V. (2020, mar). High-Order Solar Migrating Tides Quench at SSW Onsets. *Geophysical Research Letters*, *47*(6), 1–8. Retrieved from <https://doi.org/10.1029/2019GL086778> doi: 10.1029/2019GL086778
- He, M., Forbes, J. M., Jacobi, C., Li, G., Liu, L., Stober, G., & Wang, C. (2024). Observational Verification of High-Order Solar Tidal Harmonics in the Earth’s Atmosphere. *Geophysical Research Letters*, *51*(8), e2024GL108439. Retrieved 2024-04-24, from <https://onlinelibrary.wiley.com/doi/abs/10.1029/2024GL108439> (eprint: <https://onlinelibrary.wiley.com/doi/pdf/10.1029/2024GL108439>) doi: 10.1029/2024GL108439
- He, M., Forbes, J. M., Li, G., Jacobi, C., & Hoffmann, P. (2021). Mesospheric Q2DW Interactions With Four Migrating Tides at 53°N Latitude: Zonal Wavenumber Identification Through Dual-Station Approaches. *Geophysical Research Letters*, *48*(8), e2020GL092237. Retrieved from <https://doi.org/10.1029/2020GL092237> doi: 10.1029/2020GL092237
- He, M., Stober, G., & Jacobi, C. (2023). *Hourly mesospheric winds over Collm between 2012 and 2020*. Harvard Dataverse. Retrieved from <https://dataverse.harvard.edu/privateurl.xhtml?token=ba62bd31-d010-48af-b1d3-85bd8001b1d4>
- He, M., Yamazaki, Y., Hoffmann, P., Hall, C. M., Tsutsumi, M., Li, G., & Chau, J. L. (2020). Zonal Wave Number Diagnosis of Rossby Wave-Like Oscillations Using Paired Ground-Based Radars. *Journal of Geophysical Research: Atmospheres*, *125*(12). Retrieved from <https://doi.org/10.1029/2019JD031599>

doi: 10.1029/2019JD031599

- Hocking, W. K., Fuller, B., & Vandeppeer, B. (2001). Real-time determination of meteor-related parameters utilizing modern digital technology. *Journal of Atmospheric and Solar-Terrestrial Physics*, *63*(2), 155–169. Retrieved from [https://doi.org/10.1016/S1364-6826\(00\)00138-3](https://doi.org/10.1016/S1364-6826(00)00138-3) doi: 10.1016/S1364-6826(00)00138-3
- Hocking, W. K., & Kishore Kumar, G. (2011, August). Long term behaviour of the MLT quasi-7-day wave at two radar-sites at northern polar latitudes. *Journal of Atmospheric and Solar-Terrestrial Physics*, *73*(13), 1616–1628. Retrieved 2024-02-09, from <https://www.sciencedirect.com/science/article/pii/S1364682611000393> doi: 10.1016/j.jastp.2011.02.004
- Holdsworth, D. A., Reid, I. M., & Cervera, M. A. (2004). Buckland park all-sky interferometric meteor radar. *Radio Science*, *39*(5), n/a–n/a. Retrieved from <http://dx.doi.org/10.1029/2003RS003014> (RS5009) doi: 10.1029/2003RS003014
- Holton, J. R., & Hakim, G. J. (2012). *an Introduction To Dynamic Meteorology* (Vol. 41) (No. 5).
- Huang, K. M., Liu, A. Z., Zhang, S. D., Yi, F., Huang, C. M., Gan, Q., . . . Zhang, Y. H. (2013, November). A nonlinear interaction event between a 16-day wave and a diurnal tide from meteor radar observations. *Annales Geophysicae*, *31*(11), 2039–2048. Retrieved 2024-04-24, from <https://angeo.copernicus.org/articles/31/2039/2013/> doi: 10.5194/angeo-31-2039-2013
- Jacobi, C. (2012). 6 year mean prevailing winds and tides measured by VHF meteor radar over Collm (51.3N, 13.0E). *Journal of Atmospheric and Solar-Terrestrial Physics*, *78-79*, 8–18. Retrieved from <http://www.sciencedirect.com/science/article/pii/S1364682611001210> doi: <https://doi.org/10.1016/j.jastp.2011.04.010>
- Jacobi, C., Fröhlich, K., Portnyagin, Y., Merzlyakov, E., Solovjova, T., Makarov, N., . . . Kürschner, D. (2009). Semi-empirical model of middle atmosphere wind from the ground to the lower thermosphere. *Adv. Space Res.*, *43*, 239–246. doi: 10.1016/j.asr.2008.05.011
- Jacobi, C., Hoffmann, P., & Kürschner, D. (2008). Trends in mlt region winds and planetary waves, collm (52°n, 15°e). *Ann. Geophys.*, *26*(5), 1221–1232. doi: 10

.5194/angeo-26-1221-2008

- Jiang, G., Xu, J., Xiong, J., Ma, R., Ning, B., Murayama, Y., . . . Franke, S. J. (2008). A case study of the mesospheric 6.5-day wave observed by radar systems. *Journal of Geophysical Research Atmospheres*, *113*(16), 1–12. doi: 10.1029/2008JD009907
- Ma, Z., Gong, Y., Zhang, S., Xiao, Q., Huang, C., & Huang, K. (2024). Quasi-5-Day Oscillations During Arctic Major Sudden Stratospheric Warmings From 2005 to 2021. *Journal of Geophysical Research: Space Physics*, *129*(4), e2023JA032292. Retrieved 2024-04-26, from <https://onlinelibrary.wiley.com/doi/abs/10.1029/2023JA032292> (eprint: <https://onlinelibrary.wiley.com/doi/pdf/10.1029/2023JA032292>) doi: 10.1029/2023JA032292
- Matsuno, T. (1971, nov). A Dynamical Model of the Stratospheric Sudden Warming. *Journal of the Atmospheric Sciences*, *28*(8), 1479–1494. Retrieved from [http://journals.ametsoc.org/doi/abs/10.1175/1520-0469\(1971\)28<1479:ADMOTS>2.0.CO;2](http://journals.ametsoc.org/doi/abs/10.1175/1520-0469(1971)28<1479:ADMOTS>2.0.CO;2) doi: 10.1175/1520-0469(1971)028<1479:ADMOTS>2.0.CO;2
- McDonald, A. J., Hibbins, R. E., & Jarvis, M. J. (2011). Properties of the quasi 16 day wave derived from EOS MLS observations. *Journal of Geophysical Research Atmospheres*, *116*(6), 1–16. doi: 10.1029/2010JD014719
- Pancheva, D. (2001). Non-linear interaction of tides and planetary waves in the mesosphere and lower thermosphere: Observations over Europe. *Physics and Chemistry of the Earth, Part C: Solar, Terrestrial and Planetary Science*, *26*(6), 411–418. doi: 10.1016/S1464-1917(01)00022-8
- Pancheva, D., & Mitchell, N. J. (2004). Planetary waves and variability of the semidiurnal tide in the mesosphere and lower thermosphere over Esrange (68°N, 21°E) during winter. *Journal of Geophysical Research: Space Physics*, *109*(A8). doi: 10.1029/2004JA010433
- Pancheva, D., Mukhtarov, P., Mitchell, N. J., Merzlyakov, E., Smith, A. K., Andonov, B., . . . Murayama, Y. (2008). Planetary waves in coupling the stratosphere and mesosphere during the major stratospheric warming in 2003/2004. *Journal of Geophysical Research Atmospheres*, *113*(12), 1–22. Retrieved from <http://dx.doi.org/10.1029/2007JD009011> doi: 10.1029/2007JD009011

- Pogoreltsev, A. I., Fedulina, I. N., Mitchell, N. J., Muller, H. G., Luo, Y., Meek, C. E., & Manson, A. H. (2002). Global free oscillations of the atmosphere and secondary planetary waves in the mesosphere and lower thermosphere region during August/September time conditions. *Journal of Geophysical Research Atmospheres*, *107*(24), ACL 24–1–ACL 24–12. Retrieved from <https://doi.org/10.1029/2001JD001535> doi: 10.1029/2001JD001535
- Riggin, D. M., Liu, H. L., Lieberman, R. S., Roble, R. G., Russell, J. M., Mertens, C. J., ... Vincent, R. A. (2006). Observations of the 5-day wave in the mesosphere and lower thermosphere. *Journal of Atmospheric and Solar-Terrestrial Physics*, *68*(3-5), 323–339. doi: 10.1016/j.jastp.2005.05.010
- Rossby, C.-G. (1939). Relation between variations in the intensity of the zonal circulation of the atmosphere and the displacements of the semi-permanent centers of action. *Journal of Marine Research*, *2*(1), 38–55. doi: 10.1357/002224039806649023
- Salby, M. L. (1981). Rossby normal modes in nonuniform background configurations. Part II: Equinox and solstice conditions. *Journal of the Atmospheric Sciences*, *38*(9), 1827–1840. doi: 10.1175/1520-0469(1981)038<1827:RNMINB>2.0.CO;2
- Sassi, F., Garcia, R. R., & Hoppel, K. W. (2012). Large-Scale Rossby Normal Modes during Some Recent Northern Hemisphere Winters. *Journal of the Atmospheric Sciences*, *69*(3), 820–839. doi: 10.1175/jas-d-11-0103.1
- Shi, Y., Evtushevsky, O., Shulga, V., Milinevsky, G., Klekociuk, A., Andrienko, Y., & Han, W. (2021, January). Mid-Latitude Mesospheric Zonal Wave 1 and Wave 2 in Recent Boreal Winters. *Remote Sensing*, *13*(18), 3749. Retrieved 2024-05-30, from <https://www.mdpi.com/2072-4292/13/18/3749> (Number: 18 Publisher: Multidisciplinary Digital Publishing Institute) doi: 10.3390/rs13183749
- Smith, A. K. (1997, August). Stationary Planetary Waves in Upper Mesospheric Winds. *Journal of the Atmospheric Sciences*, *54*(16), 2129–2145. Retrieved 2024-05-13, from https://journals.ametsoc.org/view/journals/atsc/54/16/1520-0469_1997_054_2129_spwium_2.0.co_2.xml (Publisher: American Meteorological Society Section: Journal of the Atmospheric Sciences) doi: 10.1175/1520-0469(1997)054<2129:SPWIUM>2.0.CO;2
- Sridharan, S., Tsuda, T., Nakamura, T., Vincent, R. A., & Effendy. (2006). A Re-

- port on Radar Observations of 5-8-day Waves in the Equatorial MLT Region. *Journal of the Meteorological Society of Japan. Ser. II, 84A*, 295–304. doi: 10.2151/jmsj.84A.295
- Stober, G., Kuchar, A., Pokhotelov, D., Liu, H., Liu, H.-L., Schmidt, H., . . . Mitchell, N. (2021). Interhemispheric differences of mesosphere–lower thermosphere winds and tides investigated from three whole-atmosphere models and meteor radar observations. *Atmospheric Chemistry and Physics*, 21(18), 13855–13902. Retrieved from <https://acp.copernicus.org/articles/21/13855/2021/> doi: 10.5194/acp-21-13855-2021
- Stober, G., Liu, A., Kozlovsky, A., Qiao, Z., Kuchar, A., Jacobi, C., . . . Mitchell, N. (2022). Meteor radar vertical wind observation biases and mathematical debiasing strategies including the 3dvar+div algorithm. *Atmospheric Measurement Techniques*, 15(19), 5769–5792. Retrieved from <https://amt.copernicus.org/articles/15/5769/2022/> doi: 10.5194/amt-15-5769-2022
- Teitelbaum, H., & Vial, F. (1991, aug). On tidal variability induced by nonlinear interaction with planetary waves. *Journal of Geophysical Research: Space Physics*, 96(A8), 14169–14178. Retrieved from <http://doi.wiley.com/10.1029/91JA01019> doi: 10.1029/91ja01019
- van Caspel, W. E., Espy, P., Hibbins, R., Stober, G., Brown, P., Jacobi, C., & Kero, J. (2023). A case study of the solar and lunar semidiurnal tide response to the 2013 sudden stratospheric warming. *Journal of Geophysical Research: Space Physics*, 128(9), e2023JA031680. Retrieved from <https://agupubs.onlinelibrary.wiley.com/doi/abs/10.1029/2023JA031680> (e2023JA031680 2023JA031680) doi: <https://doi.org/10.1029/2023JA031680>
- Yamazaki, Y., & Matthias, V. (2019). Large Amplitude Quasi-10-day Waves in the Middle Atmosphere during Final Warmings. *J. Geophys. Res.*, 1–19. doi: 10.1029/2019JD030634
- Yamazaki, Y., Matthias, V., & Miyoshi, Y. (2021). Quasi-4-Day Wave: Atmospheric Manifestation of the First Symmetric Rossby Normal Mode of Zonal Wavenumber 2. *Journal of Geophysical Research: Atmospheres*, 126(13), e2021JD034855. doi: 10.1029/2021JD034855
- Yu, F. R., Huang, K. M., Zhang, S. D., Huang, C. M., Yi, F., Gong, Y., . . .

- Ning, B. (2019). Quasi 10- and 16-Day Wave Activities Observed Through Meteor Radar and MST Radar During Stratospheric Final Warming in 2015 Spring. *Journal of Geophysical Research: Atmospheres*, *124*(12), 6040–6056. Retrieved 2024-02-09, from <https://onlinelibrary.wiley.com/doi/abs/10.1029/2019JD030630> (_eprint: <https://onlinelibrary.wiley.com/doi/pdf/10.1029/2019JD030630>) doi: 10.1029/2019JD030630
- Yu, Y., Wan, W., Ning, B., Liu, L., Wang, Z., Hu, L., & Ren, Z. (2013). Tidal wind mapping from observations of a meteor radar chain in December 2011. *Journal of Geophysical Research: Space Physics*, *118*(5), 2321–2332. Retrieved from <https://agupubs.onlinelibrary.wiley.com/doi/abs/10.1029/2012JA017976> doi: 10.1029/2012JA017976
- Zaqarashvili, T. V., Albekioni, M., Ballester, J. L., Bekki, Y., Biancofiore, L., Birch, A. C., ... Yellin-Bergovoy, R. (2021). Rossby Waves in Astrophysics. *Space Science Reviews*, *217*(1), 15. Retrieved from <https://doi.org/10.1007/s11214-021-00790-2> doi: 10.1007/s11214-021-00790-2
- Zhang, X., & Forbes, J. M. (2014, dec). Lunar tide in the thermosphere and weakening of the northern polar vortex. *Geophysical Research Letters*, *41*(23), 8201–8207. Retrieved from <http://doi.wiley.com/10.1002/2014GL062103> doi: 10.1002/2014GL062103
- Zhao, Y., Taylor, M. J., Pautet, P.-D., Moffat-Griffin, T., Hervig, M. E., Murphy, D. J., ... Russell III, J. M. (2019). Investigating an Unusually Large 28-Day Oscillation in Mesospheric Temperature Over Antarctica Using Ground-Based and Satellite Measurements. *Journal of Geophysical Research: Atmospheres*, *124*(15), 8576–8593. Retrieved from <https://agupubs.onlinelibrary.wiley.com/doi/abs/10.1029/2019JD030286> doi: 10.1029/2019JD030286

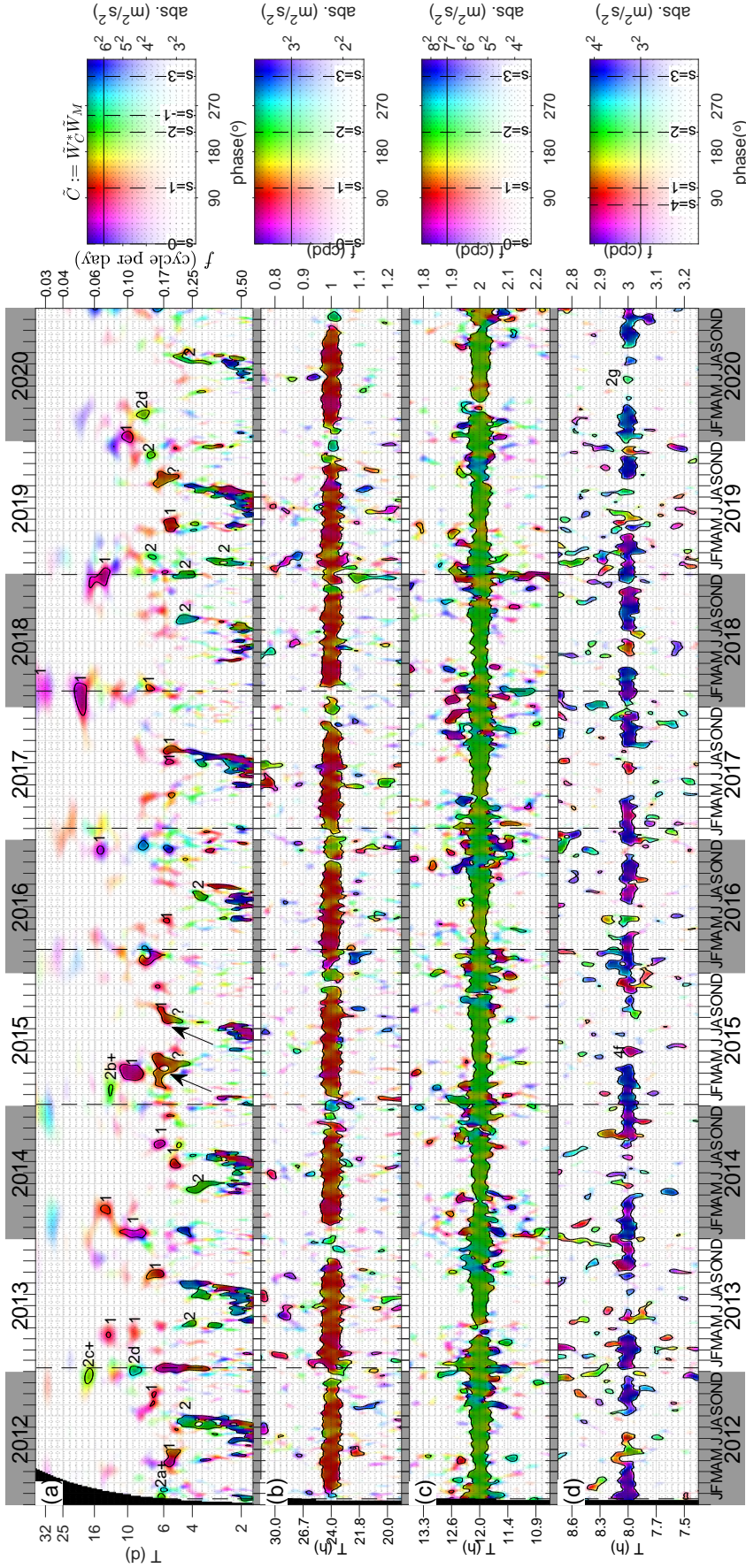


Figure 1: Altitude-averaged (80.5–95.5km) cross-wavelet spectra between Mohe and Collm across four frequency bands: (a) $f = 0.03\text{--}0.50$ cpd, (b) 1.00 ± 0.25 cpd, (c) 2.00 ± 0.25 cpd, and (d) 3.00 ± 0.25 cpd. The spectral color density indicates the magnitude of the spectra, while the hue reflects the phase difference between our Mohe and Collm stations. The color density of the spectra denotes the spectral magnitude while the colour denotes the phase difference between our Mohe and Collm stations, which is a function of the zonal wavenumber s of the underlying wave and longitudinal separation between our Mohe and Collm stations. Arabic numerals (1, 2, 3, etc.) denote nearby spectral peaks, representing the estimated zonal wavenumber s of associated underlying waves. Letters 'a+', 'b+', etc., following some Arabic numerals indicate spectral peaks resulting from nonlinear interactions specified in Lines (a+), (b+), etc., in Table 1. In each panel, the solid black and white lines represent two reference isolines, either specified by the horizontal line in the corresponding colormap or by the white number on the isolines when the isoline is saturated in the colormap.

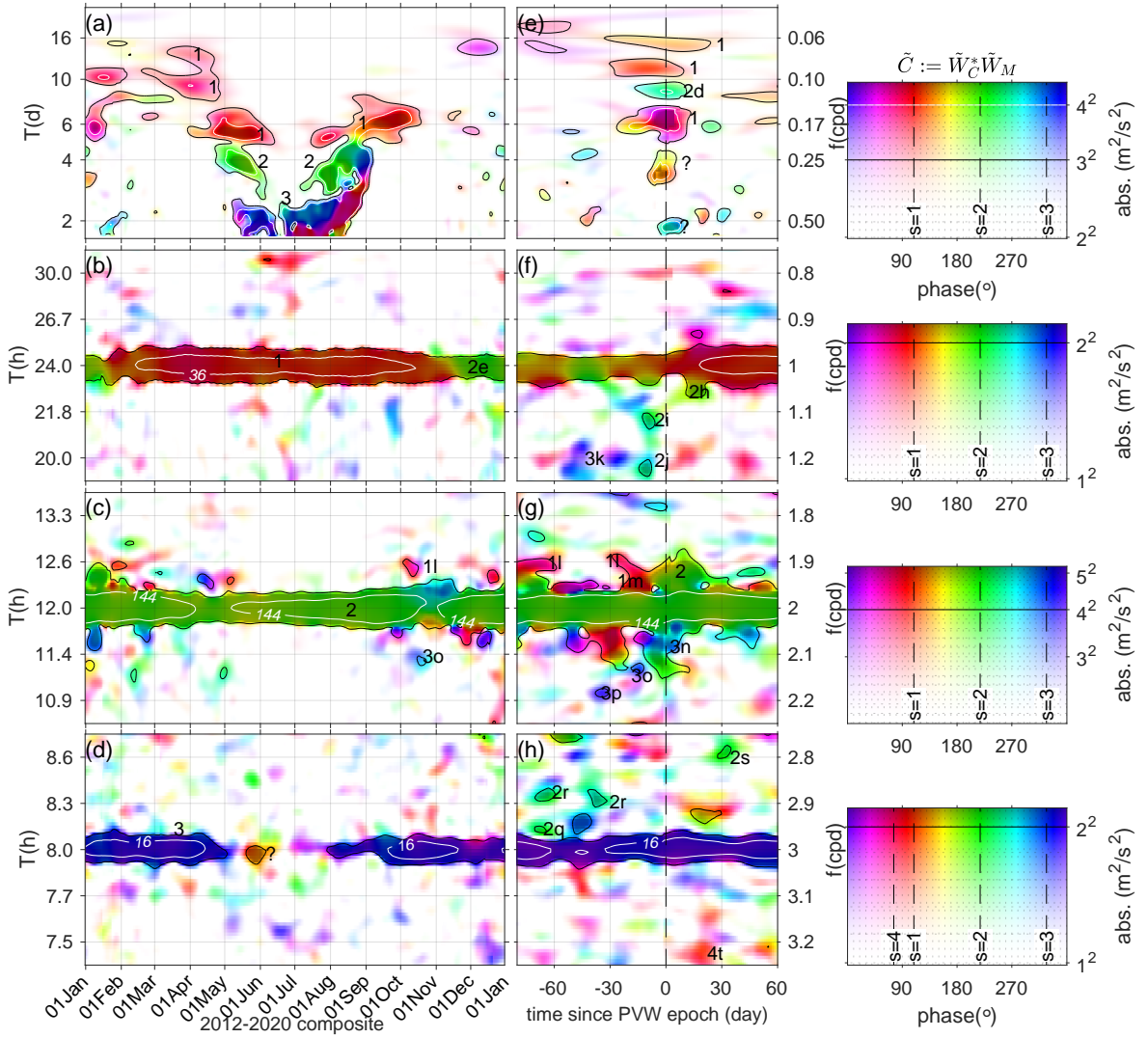


Figure 2: Composite analysis of spectra displayed in Figure 1a with respect to (a) day of year and (e) the central day of SSWs. Panels (b,f), (c,g), and (d,h) show similar plots to (a,e) but for the near-24h, -12h, and -8h spectra displayed in Figures 1b, 1c and 1d, respectively. Arabic numerals (1, 2, 3, etc.) annotate spectral peaks, representing the estimated zonal wavenumber s of associated underlying waves. Letters 'd', 'e', etc., following the numerals denote annotated spectral peaks resulting from nonlinear interactions as detailed in Lines (d), (e), etc., in Table 1. The question symbols "?" indicate spectral peaks that are attributable to superpositions of waves with multiple zonal wavenumbers See section 4 for details. In each panel, the solid black and white lines represent two reference isolines, either specified by the horizontal line in the corresponding colormap or by the white number on the isolines when the isoline is saturated in the colormap.

Table 1: Novel Findings versus Established Phenomena: Ground-Observed Nonlinear Interactions Among Atmospheric Planetary-Scale Waves

Index	PDT Results $[\frac{f}{1_{cpd}}, s]$	Explainable Alias	Potential Interactions: $[\frac{f_1}{1_{cpd}}, s_1] \pm [\frac{f_2}{1_{cpd}}, s_2] = [\frac{f_3}{1_{cpd}}, s_3]$	f Matching Evidence	Evidence for f and s Matching
(a+)	$[\frac{1}{6}, 2]$		$[\frac{1}{6}, 1] + [0, 1] = [\frac{1}{6}, 2]$		
(a-)		$[\frac{1}{6}, -1]$	$[\frac{1}{6}, 1] - [0, 2] = [\frac{1}{6}, -1]$	Meaningless	First-time disclosure
(b+)	$[\frac{1}{10}, 2]$		$[\frac{1}{10}, 1] + [0, 1] = [\frac{1}{10}, 2]$		
(b-)		$[\frac{1}{10}, -1]$	$[\frac{1}{10}, 1] - [0, 2] = [\frac{1}{10}, -1]$	Meaningless	First-time disclosure
(c+)	$[\frac{1}{16}, 2]$		$[\frac{1}{16}, 1] + [0, 1] = [\frac{1}{16}, 2]$		
(c-)		$[\frac{1}{16}, -1]$	$[\frac{1}{16}, 1] - [0, 2] = [\frac{1}{16}, -1]$	Meaningless	He, Forbes, et al. (2020) First-time proposed
(d)	$[\frac{1}{8}, 2]$		$[\frac{1}{16}, 1] + [\frac{1}{16}, 1] = [\frac{1}{8}, 2]$	He and Forbes (2022)	He and Forbes (2022)
(e)	$1, 2]$		$1, 1] + [0, 1] = [1, 2]$	Meaningless	First-time disclosure
(f)	$3, 4]$		$3, 3] + [0, 1] = [3, 4]$	Meaningless	First-time disclosure
(g)	$3, 2]$		$3, 3] - [0, 1] = [3, 2]$	Meaningless	First-time disclosure
(h)	$[\frac{24}{226}, 2]$		$[1, 1] + [\frac{1}{16}, 1] = [\frac{24}{226}, 2]$	Huang et al. (2013)	First-time disclosure
(i)	$[\frac{24}{218}, 2]$		$[1, 1] + [\frac{1}{10}, 1] = [\frac{24}{218}, 2]$		First-time disclosure
(j)	$[\frac{24}{206}, 2]$		$[1, 1] + [\frac{1}{6}, 1] = [\frac{24}{206}, 2]$		First-time disclosure
(k)	$[\frac{24}{206}, 3]$		$[1, 2] + [\frac{1}{6}, 1] = [\frac{24}{206}, 3]$	Teitelbaum and Vial (1991)*	First-time disclosure
(l)	$[\frac{24}{124}, 1]$		$[2, 2] - [\frac{1}{16}, 1] = [\frac{24}{124}, 1]$	Pancheva and Mitchell (2004)	He, Chau, Hall, et al. (2018)
(m)	$[\frac{24}{16}, 1]$		$[2, 2] - [\frac{1}{10}, 1] = [\frac{24}{16}, 1]$	Pancheva and Mitchell (2004)	He, Chau, et al. (2020)
(n)	$[\frac{24}{16}, 3]$		$[2, 2] + [\frac{1}{16}, 1] = [\frac{24}{16}, 3]$	Pancheva (2001)	He, Chau, Stober, et al. (2018)
(o)	$[\frac{24}{144}, 3]$		$[2, 2] + [\frac{1}{10}, 1] = [\frac{24}{144}, 3]$	Pancheva (2001)	He, Chau, et al. (2020)
(p)	$[\frac{24}{111}, 3]$		$[2, 2] + [\frac{1}{6}, 1] = [\frac{24}{111}, 3]$	Pancheva (2001)	First-time disclosure
(q)	$[\frac{24}{82}, 2]$		$[3, 3] - [\frac{1}{16}, 1] = [\frac{24}{82}, 2]$	First-time disclosure	First-time disclosure
(r)	$[\frac{24}{83}, 2]$		$[3, 3] - [\frac{1}{10}, 1] = [\frac{24}{83}, 2]$	First-time disclosure	First-time disclosure
(s)	$[\frac{24}{83}, 2]$		$[3, 3] - [\frac{1}{6}, 1] = [\frac{24}{83}, 2]$	First-time disclosure	First-time disclosure
(t)	$[\frac{24}{76}, 4]$		$[3, 3] + [\frac{1}{6}, 1] = [\frac{24}{76}, 4]$	First-time disclosure	First-time disclosure

*The spectral analysis in Teitelbaum and Vial (1991) did not discern between these interactions (i), (j) and (k), even only in the frequency domain. By integrating zonal

wavenumber diagnosis and ensuring proper frequency resolution, our current work distinguishes between these interactions.